



The effect of hydrogen enrichment, flame-flame interaction, confinement, and asymmetry on the acoustic response of a model can combustor



Eirik Æsøy^{a,*}, Thomas Indlekofer^b, Francesco Gant^c, Alexis Cuquel^c, Mirko R. Bothien^{a,d}, James R. Dawson^a

^a Department of Energy and Process Engineering, Norwegian University of Science and Technology, Trondheim N-7491, Norway

^b SINTEF Energy Research, Trondheim N-7465, Norway

^c Ansaldo Energia, Baden, Switzerland

^d Institute of Energy Systems and Fluid Engineering, Zürich University of Applied Sciences ZHAW, Zürich, Switzerland

ARTICLE INFO

Article history:

Received 27 September 2021

Revised 26 April 2022

Accepted 27 April 2022

Keywords:

Flame dynamics
Flame transfer function
Interacting flames
Asymmetry
Hydrogen

ABSTRACT

To maximise power density practical gas turbine combustion systems have several injectors which can lead to complex interactions between flames. However, our knowledge about the effect of flame-flame interactions on the flame response, the essential element to predict the stability of a combustor, is still limited. The present study investigates the effect of hydrogen enrichment, flame-flame interaction, confinement, and asymmetries on the linear and non-linear acoustic response of three premixed flames in a simple can combustor. A parametric study of the linear response, characterised by the flame transfer function (FTF), is performed for swirling and non-swirling flames. Flame-flame interactions were achieved by changing the injector spacing and the level of hydrogen enrichment by power from 10 to 50%. It was found that the latter had the most significant effect on the flame response. Asymmetry effects were investigated by changing one of the flames by using a different bluff-body to alter both the flame shape and flow field. The global flame response showed that the asymmetric cases can be reconstructed using a superposition of the two symmetric cases where all three bluff-bodies and flames are the same. Overall, the linear response characterised by the flame transfer function (FTF) showed that the effect of increasing the level of hydrogen enrichment is more pronounced than the effect of the injector spacing. Increasing hydrogen enrichment results in more compact flames which minimises flame-flame interactions. More compact flames increase the cut-off frequency which can lead to self-excited modes at higher frequencies. Finally, the non-linear response was characterised by measuring the flame describing function (FDF) at a frequency close to a self-excited mode of the combustor for different injector spacings and levels of hydrogen enrichment. It is shown that increasing the hydrogen enrichment leads to higher saturation amplitude whereas the effect of injector spacing has a comparably smaller effect.

© 2022 The Author(s). Published by Elsevier Inc. on behalf of The Combustion Institute. This is an open access article under the CC BY license (<http://creativecommons.org/licenses/by/4.0/>)

1. Introduction

In light of increasing environmental concerns, industry faces a continuing need to reduce green house gas emissions. By introducing fuel blends with high quantities of hydrogen, gas turbines can significantly reduce carbon dioxide emissions and play a major role in the integration of intermittent renewable energy sources. However, the high reactivity of hydrogen changes the flame properties and can alter the operational stability limits of a gas turbine

by promoting flashback and combustion instabilities [1]. This paper focuses on the latter problem. The addition of hydrogen can be stabilising [2–4] or destabilising [5–14] depending on the mode of combustion and the level of enrichment.

Combustion instabilities arise from a constructive coupling between the acoustics, flow and the fluctuating heat release rate in the combustor [15]. The resulting pressure fluctuations can cause increased heat transfer to the walls, vibrations and in the worst outcome catastrophic failure. Understanding the response of flames to acoustic perturbations over a range of frequencies and amplitudes is crucial to our ability to predict them. A common approach to characterise the linear flame response is to obtain the

* Corresponding author.

E-mail address: eirik.asoy@ntnu.no (E. Æsøy).

flame transfer function (FTF), which is usually done experimentally [16–19], but can be done using numerical simulations [20] or analytically modeled in the case of simple flames [21–25]. The non-linear response of the flame, i.e. the saturation amplitude, can be obtained by measuring at a range of forcing amplitudes at frequencies of interest resulting in a flame describing function (FDF) [26–28].

A common feature of premixed flames is that they behave as a low-pass filter where the gain drops exponentially after a cut-off frequency determined by the convective compactness of the flame. This convective compactness is given by the ratio of the characteristic flame length and the flow velocity. It also provides the slope of the FTF phase with the frequency, being indicative of a constant convective time-delay [21]. It has recently been shown that hydrogen enrichment reduces the flame length, producing more compact flames, which increases the cut-off frequency and reduces the time delay [5,13,19,29,30].

FTFs and FDFs are usually measured for single flames. However, it is known that flame-flame and flame-wall interactions as well as heat transfer can change the mean flame shape and thereby the response [18,31–34]. These effects are all in play in gas turbine combustors where multiple injectors are arranged around an annulus (annular combustor) or in an array of several injectors in cans (can-annular combustor). Flame-flame interactions with two bluff-body stabilised flames, subjected to self-excited and forced instabilities were studied by Worth and Dawson [35, 36]. Both frequency and stability of the self excited instabilities were found to be affected by a change in flame separation distance. Several studies have also investigated the effects of flame-flame interactions on the flame structure [37–39]. Lee et al. [40] investigated two interacting swirling flames and found that both the FTF and the FDF were sensitive to the swirl direction, implying that the use of single flame data for the prediction of the multi flame dynamics can lead to erroneous results. In the same setup, a staggered swirler arrangement (swirlers placed at different axial positions) was found to have a strong effect on the stability map of the combustion system [41]. The effect of symmetry breaking by means of different equivalence ratios of the two flames (fuel staging) was also investigated [42] and the stability was found to be very sensitive to the fuel-split conditions. A single can combustor with five injectors, a configuration based on industrial applications, was introduced by Szedlmayer et al. [43]. At very low frequencies, the gain for a single flame reference case was larger compared to the multiple flame configuration, while it was the opposite for slightly higher frequencies. At moderate frequencies, the response was very similar and at higher frequencies the gain of the multi-nozzle flame was slightly higher. This displays the complexity of the flame response for multiple flames in a can combustor. In a similar set-up, Samarasinghe et al. [44] used a tomographic image reconstruction technique to obtain the 3D structure of the interacting flames, revealing the complex structure in the interaction zones between adjacent flames. In the same combustor, the effect of fuel staging on the stability of the system was investigated [45]. When the asymmetry in the fuel staging was increased, the distribution of the time-averaged heat release rate changed in the regions where adjacent flames interact, reducing the amplitudes of heat release rate fluctuations in those regions.

So far, the influence of hydrogen enrichment on the response in similar multiple flame systems remains largely unexplored. The present study addresses this issue by focusing on the linear and non-linear flame response in a multi-injector burner with varying degrees of hydrogen enrichment. The experimental setup and methods are described in Section 2. Then, the effect of flame-flame interaction, varied through hydrogen enrichment and the physical spacing of the injectors, the effect of confinement and asymmetric injector configurations are investigated for both non-swirled and

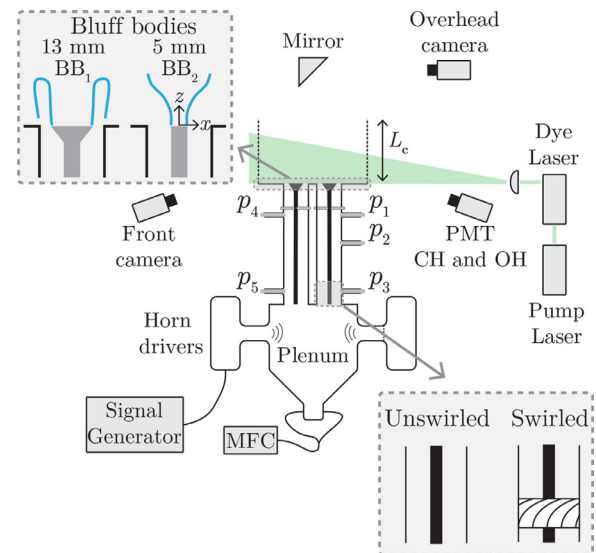


Fig. 1. Schematic of the experimental setup showing the diagnostic and geometries considered. In the gray boxes the dump plane geometries and upstream flow conditioning are shown.

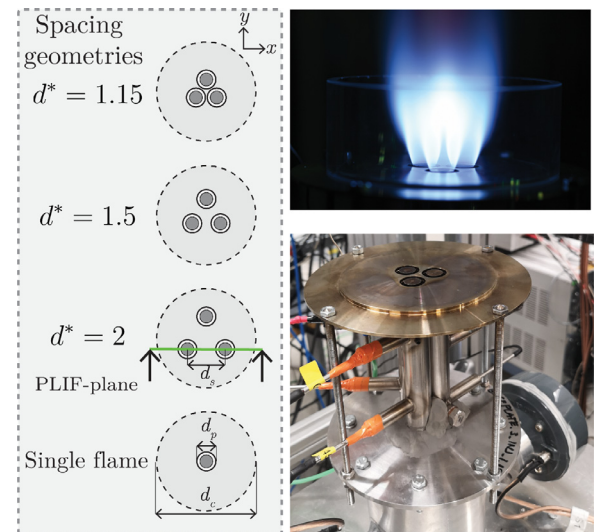


Fig. 2. Photographs of three flames (top) operated at $P_H = 0.1$ and the base plate (bottom) for $d^* = 1.15$. The gray box shows the spacing configurations considered in the paper, viewed from above, and the plane investigated with OH-PLIF.

swirled flames in Section 3. In Section 4 the effect of hydrogen enrichment and flame-flame interaction on the non-linear flame response is investigated for forced and self-excited instabilities.

2. Experimental setup and methods

2.1. Experimental setup

Figs. 1 and 2 show a schematic of the experimental setup and a top view of the burner geometry. The geometry consists of a circular combustion chamber of diameters $d_c = [120, 90, 44]$ mm with variable lengths $L_c = [50, 100, 200]$ mm. A single flame or three flames are stabilised on bluff-bodies with diameters $d_b = 13$ mm (BB_1) or $d_b = 5$ mm (BB_2) respectively, centered at the exit of the injector pipes of diameter $d_p = 19$ mm. Each injector can be equipped with a six-vane axial swirler where the trailing edge of the swirler is located 130 mm upstream of the dump plane. The injectors are connected to a cylindrical plenum. Apart from increas-

ing the number of flames, the geometry upstream of the dump plane is identical to the previous studies [13,19,29,46].

For the setup with three flames, the spacing between adjacent flames can be varied by three holder plates with normalised separation distances $d^* = d_s/d_p = [1.15, 1.5, 2]$. These are shown in Fig. 2 and are similar to the values of d^* studied by Worth and Dawson [35]. The choice of three injectors was based on the simplicity of modifying the combustor from previous experiments. It allows similar distances to the study with two flames by Worth and Dawson [35] without changing the geometry upstream of the injectors and operation of the experiment on the single sector test bench (more injectors would have required modifications of the gas supply system). Also, it is the lowest number of flames that provides symmetry with a circular enclosure, where all flames experience similar wall-flame and flame-flame interaction. This makes it different from the circular combustors with 5 injectors where the center flame experiences significantly more interaction than the other flames [43,45].

Premixed mixtures of hydrogen, methane and air are fed through the injectors from the plenum. Each of the gases is controlled by an Alicat mass flow controller. On the side wall of the plenum two Monacor KU-516 horn drivers driven by a QTX Sound PRO1000 power amplifier are mounted to provide acoustic forcing. The forcing signal p_{ref} is generated using an Aim-TTi TGA1244 signal generator.

2.2. Operating conditions

To investigate the effect of flame-flame interaction on the acoustic flame response, three mixtures of different hydrogen power content $P_H = [0.1, 0.3, 0.5]$ are considered. These correspond to volume fractions of $V_H = [0.25, 0.56, 0.75]$ where P_H and V_H are defined as

$$P_H = \frac{P_{H_2}}{P_{H_2} + P_{CH_4}} \quad V_H = \frac{V_{H_2}}{V_{H_2} + V_{CH_4}}. \quad (1)$$

P_{H_2} and P_{CH_4} are the thermal powers of hydrogen and methane, and V_{H_2} and V_{CH_4} are the volume flow rates of hydrogen and methane in the corresponding mixture. The power is kept fixed at $P = 7$ kW per flame at a fixed equivalence ratio of $\Phi = 0.7$. This gives a total power of 21 kW for the experiments with three injectors and 7 kW with one injector. Fixing Φ and changing P_H provides an approximately constant bulk velocity $\bar{u}_p \approx 11.4$ m/s ($\pm 2.5\%$) inside the injector pipes. With addition of the 13 mm bluff-body (BB_1), the bulk velocity at the exit increases to $\bar{u} \approx 20$ m/s due to the additional area blockage.

The similar bulk velocities for different values of P_H reduce the effect of different convection speeds and allows to study the effect of changing the flame-flame interaction due to a change of the flame speed in isolation. Subsequently the level of interaction is changed in two ways: 1) the separation distance is fixed and the fuel mixture is changed and 2) the fuel mixture is fixed and the separation distance is changed. The effect of swirl is also investigated for a number of conditions, all summarised in Table 1.

The effect of wall confinement was also investigated by changing the diameter of the combustion chamber while keeping all other parameters fixed. This was investigated for the single flame and for $d^* = 2$ with $P_H = 0.5$.

We also investigated the effect of having a collection of differently sized bluff-body stabilised flames, i.e. various combinations of BB_1 and BB_2 . Due to the difference in the contraction ratio, these experience significantly different convection speeds which have a major effect on the flame response. The response of asymmetric combinations is compared against symmetric collections consisting of only BB_1 or BB_2 type bluff-bodies. In configurations with both BB_1 and BB_2 , small changes in the power occur as each injector

Table 1

Operating conditions of the experiments performed in this study. The first two columns describe the normalised separation distance d^* and the hydrogen power fraction P_H . The next three columns indicate how many injectors were equipped with a 13 mm bluff-body (BB_1), the 5 mm bluff-body (BB_2), or swirlers (SW), and the last two columns show the combustion chamber diameter d_c and length L_c . For all cases, the thermal power is kept fixed at $P = 7$ kW per burner with an equivalence ratio of $\Phi = 0.7$.

d^*	P_H	BB_1	BB_2	SW	d_c [mm]	L_c [mm]
[–]	0.1,0.3,0.5	1	0	0	120	50
[–]	0.5	1	0	0	44,90,120	50,100,200
[–]	0.5	1	0	1	120	50
[–]	0.5	0	1	0	120	50
2	0.1,0.3,0.5	3	0	0	120	50,100,200
2	0.5	3	0	0	90,120	50
2	0.5	3	0	3	120	50
2	0.5	2	1	0	120	50
2	0.5	1	2	0	120	50
2	0.5	0	3	0	120	50
1.5	0.1,0.3,0.5	3	0	0	120	50,100,200
1.5	0.5	3	0	3	120	50
1.15	0.1,0.3,0.5	3	0	0	120	50,100,200
1.15	0.5	3	0	3	120	50

is fed from a common plenum. The small difference in the pressure drop leads to a small difference in the flow rates and hence, a small difference in the power of each flame. These differences were estimated by examining the overhead images of the flames. The mean images were divided into three sectors to estimate the HRR per flame, which were compared against the flow rate obtained by a simple pipe network analysis (see Appendix A). For cases with the same bluff-bodies, the difference was less than 5%, and with different bluff-bodies the difference was less than 20% for all cases.

2.3. Instrumentation and data acquisition

The pressure p was measured with Kulite XCS-093-0.35D pressure transducers mounted flush at three axial locations in injector pipe A and two axial locations in B and C as indicated in Fig. 1. Pressure signals were conditioned by an amplifier (Fylde FE-579-TA), and stored at a sampling rate of 51.2 kHz. Signals were digitised by a 24-bit DAQ system (NI-9234).

Two Hamamatsu H11902-113 photomultiplier tubes (PMT) equipped with UV band pass filters, 310 ± 10 nm for OH^* and 430 ± 10 nm for CH^* , were used to estimate the global HRR at the same temporal resolution as the pressure measurements. Since the air-fuel mixture can be considered perfectly premixed, the chemiluminescence intensity is proportional to the global HRR ($I/\bar{I} = Q/\bar{Q}$) [47].

Images of OH^* -chemiluminescence were obtained from the front and top using two Phantom V2012 high speed cameras equipped with LaVision Intensified Relay Optics (IRO) units with Cerco 2178 UV lenses (100F/2.8) and UV filters (310(10)nm). Fig. 3 shows that the resulting time-series from the PMT and camera are in very close agreement. Since these provide three different views of the flame with different lines of sight as well as with and without the quartz section, the relative effects of signal trapping or optical degradation of the quartz can be considered negligible. The images and PMT signals are normalised such that spatial integration provides the thermal power, i.e. $P = \bar{I} = \int_V q dV$. This ensures that all images can be compared with the same intensity scale. It should be mentioned that the method only provides an estimate of the HRR.

To obtain planar views of the interacting flame fronts, OH-PLIF was used. A 100 W green (532 nm wavelength) Edgewave laser pumping a Sirah Credo-Dye-N laser beam of 3 W where the output wavelength was tuned to match the absorption peak of the OH-radicals at 281 nm. The ≈ 1 mm thick and ≈ 50 mm high laser

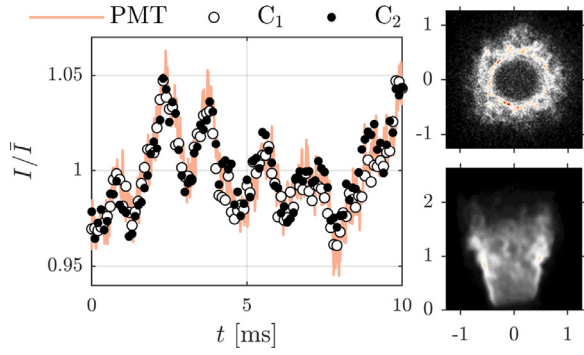


Fig. 3. Snapshot of the flame taken from the front (C_1) and side (C_2) cameras. Integrating these provides time series of the global OH^+ -chemiluminescence (I/\bar{I}) which is in agreement with the PMT signal.

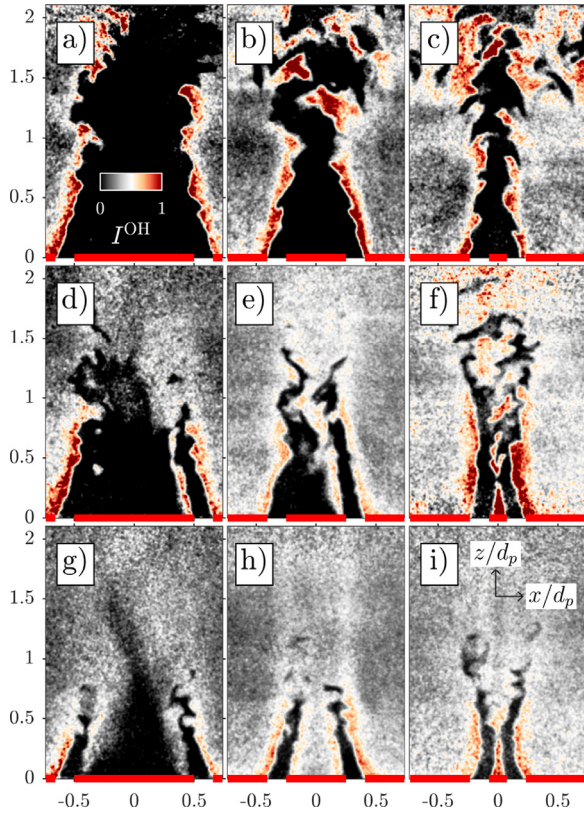


Fig. 4. Snapshots of normalised OH-PLIF images in the region between two adjacent unswirled flames with BB_1 . Top row shows from left to right $d^* = [2, 1.5, 1.15]$ for $P_H = 0.1$ (a,b,c), for $P_H = 0.3$ (d,e,f) and for $P_H = 0.5$ (g,h,i). The flame front position is located close the edges in the images where the OH intensity gradient (∇I^{OH}) is high.

sheet is aligned to cut two adjacent flames through the center of the bluff-bodies (see Figs. 2 and 4). All images are taken at a rate of 10kHz. The flame front position is located close the edges in the images where the OH intensity gradient (∇I^{OH}) is high [27,35].

2.4. Calculation of the acoustic field

The pressure time series are used to reconstruct the 1D acoustic field inside the injector pipes which is described by

$$\hat{p}_a(z) = A^+ \exp(-jk_+z) + A^- \exp(jk_-z) \quad (2a)$$

$$\hat{u}_a(z) = \frac{1}{\rho c} (A^+ \exp(-jk_+z) - A^- \exp(jk_-z)), \quad (2b)$$

where ρ and c are the gas density and the speed of sound respectively, and $k_{\pm} = k/(1 \pm \bar{u}/c)$ is the wave number $k = 2\pi f/c$. The complex amplitudes A^+ and A^- represent upstream and downstream propagating 1D acoustic waves and are obtained in each injector pipe using the Multiple Microphone Method (MMM) [48]. This allows to calculate the acoustic velocity

$$\hat{u} = \frac{A_p}{A_b} \hat{u}_a(z=0) \quad (3)$$

at the dump plane, where A_p/A_b is the ratio of the cross section areas inside the injector pipe and after the contraction of the bluff-body. For BB_1 $A_p/A_b = 1.75$, and for BB_2 $A_p/A_b = 1$. The change in area is assumed to be acoustically compact and the terms of second or higher order Mach numbers are neglected. Therefore, the effect of the bluff-body on the acoustic pressure is also neglected.

All complex amplitudes, denoted by hatted quantities ($\hat{\cdot}$), are calculated by

$$\hat{Q} = \frac{\text{PSD}(p_{\text{ref}}, Q')}{\sqrt{\text{PSD}(p_{\text{ref}} \cdot p_{\text{ref}})}}, \quad (4)$$

where PSD denotes the energy spectra estimated using the Welch method from an average of 50% overlapping windows.

2.5. Calculation of the flame transfer function (FTF)

The flame response to acoustic forcing is quantified through the flame transfer function (FTF) given by

$$\text{FTF}(\omega) = \frac{\hat{Q}/\bar{Q}}{\hat{u}/\bar{u}} = G \exp(j\theta), \quad (5)$$

which relates the normalised fluctuations of heat release rate to the normalised fluctuations of acoustic velocity. The response is represented by a complex number where G gives the magnitude and θ gives the phase. For the cases where three flames are present, the FTF is estimated from the average value of $\hat{u} = \frac{1}{3} \sum_{i=1}^3 \hat{u}_i$. FTFs are measured in the linear regime at a constant forcing level $|\hat{u}|/\bar{u} = 0.05$ for all operating conditions listed in Table 1 at frequencies $f = [50 - 2000]$ Hz.

To investigate the non-linear response, Flame describing functions (FDFs) were measured at $f = 1000\text{Hz}$. The definitions of the FDF and FTF are the same, but now the response is also a function of the forcing amplitude $|\hat{u}|/\bar{u}$. The frequency $f = 1000\text{Hz}$ was chosen because it aligns with a resonance of the rig which allows for high forcing amplitudes. Furthermore, a self excited instabilities occurred at this frequency.

To analyse and extract physical parameters from the measured FTFs, we use a distributed time lag model introduced in [19]:

$$\text{DTL}(\omega) = \frac{g}{2} \left(e^{-\frac{1}{2}(\omega+\beta)^2\sigma^2} + e^{-\frac{1}{2}(\omega-\beta)^2\sigma^2} \right) e^{-j\omega\tau}. \quad (6)$$

Here g , β and σ are model parameters that control the amplitude, location of the peak and the width of the distribution, and τ is the corresponding time delay. The model parameters are obtained by fitting the measured transfer functions to Eq. (6) with the constraint that $|\text{DTL}(0)| = 1$ giving $g = e^{(\frac{1}{2}\beta^2\sigma^2)}$ [49].

From the model parameters we extract the gain cut-off frequency defined as

$$|\text{DTL}(\omega_c)| = \frac{g}{2\sqrt{2}}. \quad (7)$$

3. The linear response

In this section we present the parametric study of the linear flame response (FTF).

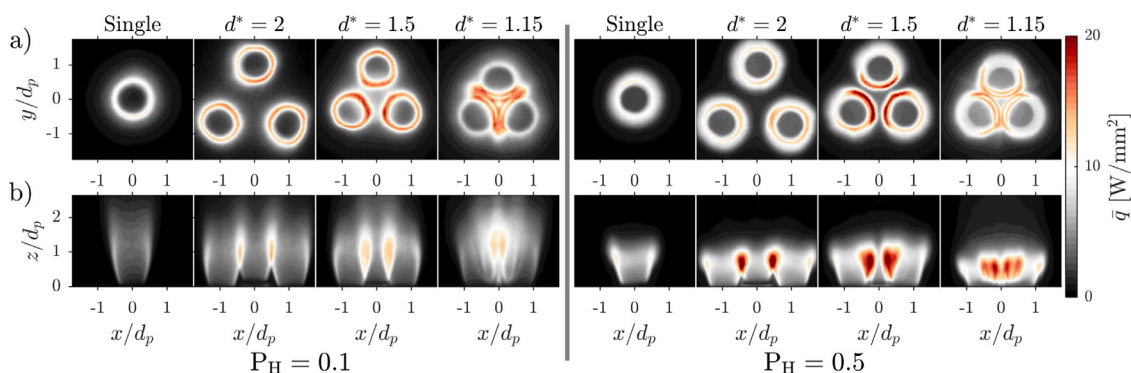


Fig. 5. Time averaged flame images taken from the top (a) and the side (b) for different separation distances S . All images are normalised such that the spatial integral gives the thermal power.

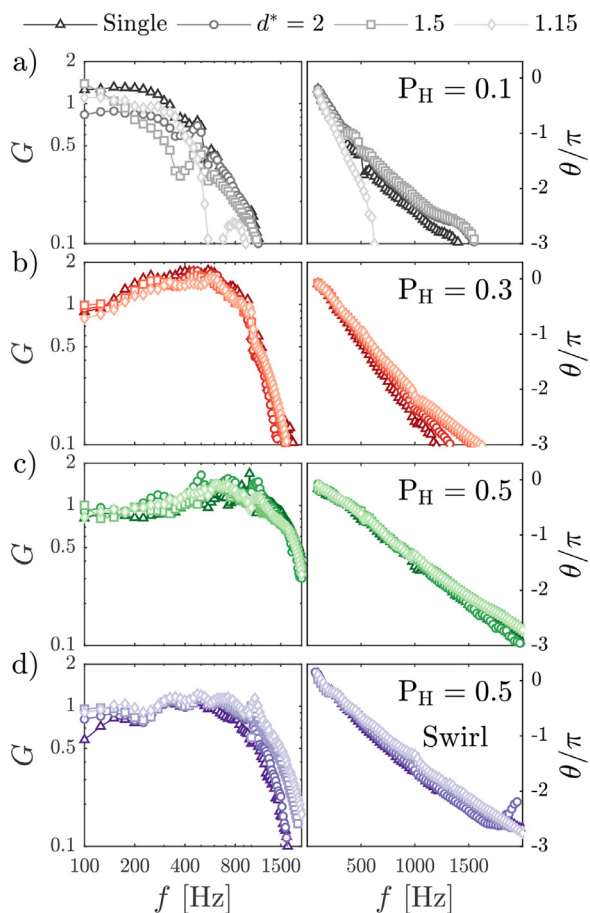


Fig. 6. FTFs for $P_H = 0.1, 0.3, 0.5$ without swirl (a-c) and with swirl for $P_H = 0.5$ (d). The left column shows the gain G and the right column shows the phase θ . The gain G is displayed in log-log and the phase in linear-linear scales to highlight the low-pass and linear time delay behaviour respectively.

3.1. Effect of interaction, swirl, and fuel composition

As already mentioned, the level of flame-flame interaction is varied in two ways, either by the flame spacing or the fuel composition. Both effects are shown in Fig. 4 by snapshots of OH-PLIF images for cases without swirl using BB_1 . Moving from the left to the right, the spacing d^* is reduced keeping P_H constant, and moving from the top to bottom, P_H is increased for a fixed spacing.

Both methods (decreasing d^* and P_H) have the effect of increasing the level of interaction between the two flame fronts. Addition-

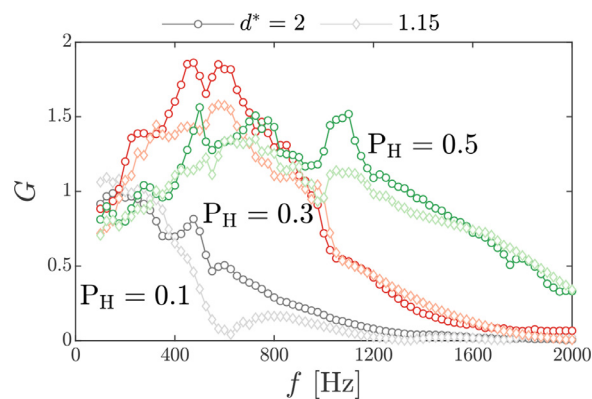


Fig. 7. Gain of the FTF displayed in a linear-linear scale for $P_H = 0.1, 0.3, 0.5$, and $d^* = 2$ and 1.15 .

ally, the increase of P_H leads to significantly shorter flames. The increased interaction for larger P_H is a result of the flames tendency to stabilise on the outer rim of the injector pipe as a "M" shaped flame. This effect is enhanced by the presence of the adjacent flame front which can be viewed for both $P_H = 0.3$ and 0.5 when d^* is reduced.

Fig. 4 only shows the flames viewed in the interaction zone between two adjacent injectors. To get a global view, the average HRR is shown for $P_H = 0.1$ and $P_H = 0.5$ in Fig. 5, where a) and b) show the top and side views, for different d^* of the unswirled flame configuration, respectively.

The single flame case is shown in the left column and for both blends, the three flames at $d^* = 2$ are very similar to the single flame, viewed from the top (a). Hence, the level of interaction between the flames at this spacing is small, as also seen by the PLIF images in Fig. 4. As the flames are moved closer together, the distribution of \bar{q} changes significantly in the top plane. At $d^* = 1.5$ the HRR increases in the region between adjacent flames, i.e. at the center of the combustor. This is due to presence of the adjacent flame which causes mutual stabilisation of the flame on the outer injector rim forming a M-flame structure. At $d^* = 1.15$, a strong interaction zone between flames is formed for $P_H = 0.1$.

The corresponding FTFs are shown in Figs. 6 and 7. In Fig. 6 a-c), the FTFs are grouped in terms of P_H , and the swirled cases measured at $P_H = 0.5$ are shown in d). The axis of the gain G are displayed logarithmically to highlight the low-pass characteristics of the FTFs. However, this can hide differences in the gain for varying d^* in the pass-band (below the cut-off frequency). Therefore, to highlight these differences, we also show the gain of the same FTFs with linear axis in Fig. 7. To minimise clutter, this figure plots the furthest and closest flame spacings $d^* = 2$ and 1.15 for each P_H .

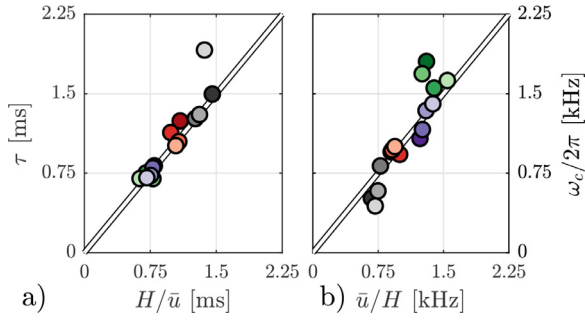


Fig. 8. Time delay τ and cut-off frequency ω_c extracted from the DTL model, plotted against H/\bar{u} for all cases shown in Fig. 6. The color of the marker matches the color of the corresponding FTF. (For interpretation of the references to color in this figure legend, the reader is referred to the web version of this article.)

Since the distribution of HRR depends significantly on the spacing, differences in the FTFs are to be expected. When $P_H = 0.1$ the FTFs show a strong variation with d^* . Compared to the single flame case, a drop in the gain is observed when $d^* = 2$, although the FTF still closely follows the same trend of the single flame. The most significant differences occur when $d^* \leq 1.5$ and are caused by the change in the flame structure in the interacting region as viewed in Fig. 5.

At each P_H , the FTFs do not collapse with d^* and there are some variations in the magnitude of the gain and the cut-off frequency. However, a general trend is that differences in the gain with varying d^* are progressively reduced for $P_H > 0.1$ compared to the $P_H = 0.1$ cases. In Fig. 7, the overall shapes of the FTFs, i.e. the regions of excess gain and the cut-off frequencies are primarily governed by P_H . The excess gain shifts to higher frequencies with increasing P_H . For a fixed P_H , the excess gain decreases slightly when the flame spacing d^* is reduced. We note that differences in the gain for a fixed P_H remain important but the main parameter affecting the gain is P_H .

As P_H is increased, the flames become shorter leading to an increase in the cut-off frequency and a shorter time delay, shown by the slope of θ . The variations with d^* , observed for $P_H = 0.1$, become less pronounced. This suggests that higher levels of hydrogen enrichment reduce the effect of flame-flame interactions, resulting in FTFs that are closer to that of a single flame.

The behaviour of the swirled cases is similar to cases without swirl, although the cut-off frequencies are slightly lower. In the following, we show that all the changes to the gain cut-off frequency and time delay can be attributed to a change of the flame height, given by the stream-wise distribution of HRR.

The flame height H , defined as the stream-wise distance from the burner exit to the centre of HRR, was computed from the side images of the flame by

$$H = \frac{\int qzdz}{\int qdz}, \quad (8)$$

and the time delay and gain cut-off frequency were obtained by fitting the data to the DTL model (Eq. (6)). These parameters are plotted against each other in Fig. 8, where a line of unity slope has been added for reference. The markers are colored according to the FTFs displayed in Fig. 6.

Both parameters (τ and ω_c) are shown to scale linearly with H and \bar{u} which is consistent with the study of single flames by Æsøy et al. [19]. In both Fig. 8a) and b) the parameters cluster closely together for flames with the same hydrogen content, showing that the flame-flame interaction affects the FTF slightly by changing the distribution of HRR and thus change the effective length of the flame. The effect of changing the hydrogen content which leads to

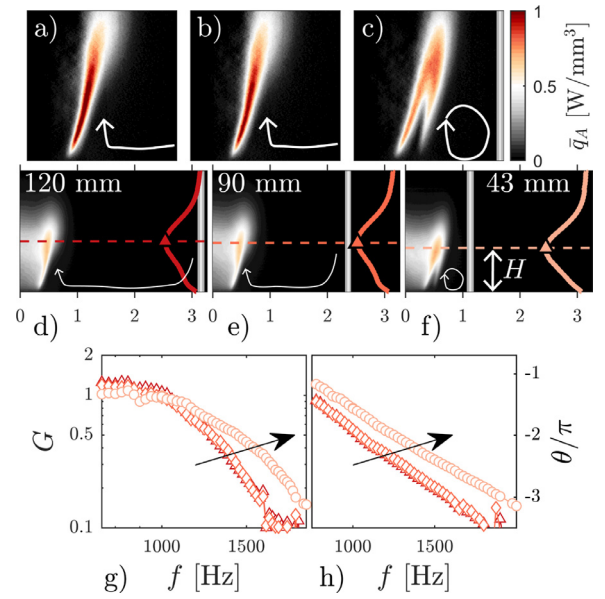


Fig. 9. The effect of confinement on the FTF for a single unswirled flame at $P_H = 0.5$ with three enclosures: 120mm, 90mm, and 44mm. The three middle (d-f) and top panels (a-c) show the line of sight and planar distribution of HRR respectively. The axis dimensions and the color scaling are the same as in Fig. 5. For the smallest enclosure, the flame attaches at the outer rim of the pipe and H is reduced by 10% due to recirculating hot combustion products. The bottom panels (g and h) show the corresponding FTFs for the three cases. (For interpretation of the references to color in this figure legend, the reader is referred to the web version of this article.)

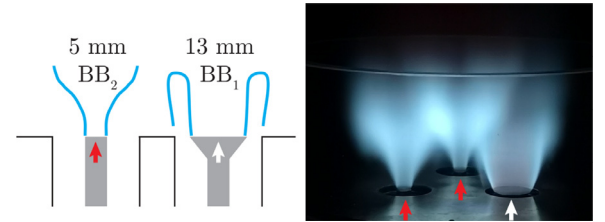


Fig. 10. Schematic and image of asymmetric configuration consisting of one 13mm (BB_1) and two 5mm (BB_2) bluff-body stabilised flames at $P_H = 0.5$.

a shorter flame, a shorter time delay, and a higher gain cut-off frequency, is significantly stronger.

3.2. Effect of confinement

For the cases shown in the previous section, the outer confinement was kept the same as d^* was varied. To investigate the effect of wall confinement on the response, the outer confinement was varied for a single unswirled flame at $P_H = 0.5$.

Figure. 9 a-f) shows the right part of the flame, for different confinements viewed from the side with the corresponding FTFs at the bottom (g-h). The middle panels (d-f) show the line of sight HRR and the top panels (a-c) show the planar distributions obtained from Abel deconvolution. The gray lines indicate the location of the wall and the stream-wise distribution, used to calculate the flame height H , is plotted on the right side of the figure.

With a combustion chamber diameter of 120mm and 90mm, the flame is not affected by the presence of the wall and the shapes are very similar. This is also confirmed by the FTFs shown at the bottom, which overlap. As the confinement is reduced to 44mm, a small but significant change to the flame shape is observed. The presence of the wall now induces recirculation of hot combustion products to the outer part of the flame, illustrated by the white lines, which then stabilise on the outer rim of the injector pipe, resulting in a "M" shaped flame as shown by the pla-

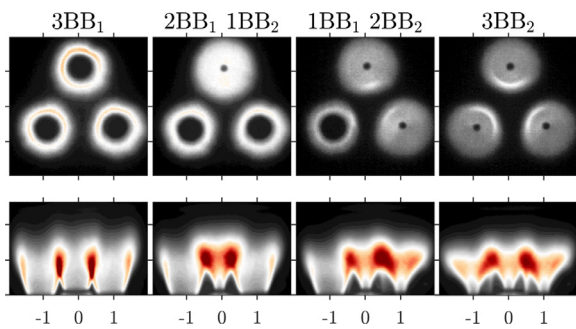


Fig. 11. Mean flame images for $P_H = 0.5$ with different combinations of bluff-bodies. The notation on top indicates the number of 13mm (BB_1) and 5mm (BB_2) bluff-body stabilised flames. The axis dimensions and the color scaling are the same as in Fig. 5. (For interpretation of the references to color in this figure legend, the reader is referred to the web version of this article.)

nar distributions Fig. 9c). This leads to a change of the stream-wise HRR and a 10% shorter flame length, similar to what was observed for interacting flames. As such, the time delay is decreased and the gain cut-off frequency is increased which is indicated by the two arrows in the FTF plots (g-h). The same was observed for cases with three flames using $d_c = 120\text{mm}$ and $d_c = 90\text{mm}$ with $d^* = 2$, which is not shown here for brevity. These results are consistent with De Rosa et al. [33] who also reported that flame-wall interaction altered the FTF through changing the distribution of the HRR.

3.3. Effect of asymmetry

In the previous section it was shown that interaction between adjacent flames and confinement can have an effect on the distribution of the stream-wise HRR and therefore, the linear response of the flame, modifying the mean time delay and the cut-off frequency. In this section we induce a significant asymmetry on the flame by changing the convection speed of adjacent flames separately. This is achieved by combining injectors equipped with both BB_1 and BB_2 type bluff-bodies, thereby inducing different bulk velocities at the dump plane. A schematic and an image of the flames are shown in Fig. 10 where one BB_1 and two BB_2 bluff-body stabilised flames are present.

Systematic measurements were conducted for all combinations of BB_1 and BB_2 , and the mean flame shapes are shown in Fig. 11. Seen from the top, there is a significant difference between the flame produced by BB_1 and BB_2 in terms of the distribution of HRR. Despite the significant differences in the top view, the stream-wise distribution, i.e. the flame length, is not affected significantly. Nonetheless, due to the change of the bulk velocity, the time delay and cut-off frequency of the response are changed, as is shown for the cases with only $3 \times BB_1$ or $3 \times BB_2$ stabilised flames in Fig. 12. The time delay of the BB_2 -stabilised flames is 1.75 times larger than the time delay of the BB_1 -stabilised flames which affects the steepness of the phase in the FTFs shown in Fig. 13a).

In Fig. 13 b) and c) the measurements are shown for the two asymmetric cases using both bluff-bodies simultaneously. The response now contains modulations similar to those measured in single flames with acoustic/convective interference [19,29,46,50,51]. This indicates that a similar phenomenon occurs, now between the adjacent flames with different time delays.

Using the DTL model for the two symmetric cases, the response of an asymmetric collection of flames can be represented as a superposition of the symmetric cases. This is shown in Fig. 13 b) and c) by the solid lines, which are obtained by

$$DTL_a = \frac{n_{BB_1} DTL_{BB_1} + n_{BB_2} DTL_{BB_2}}{n_{BB_1} + n_{BB_2}}, \quad (9)$$

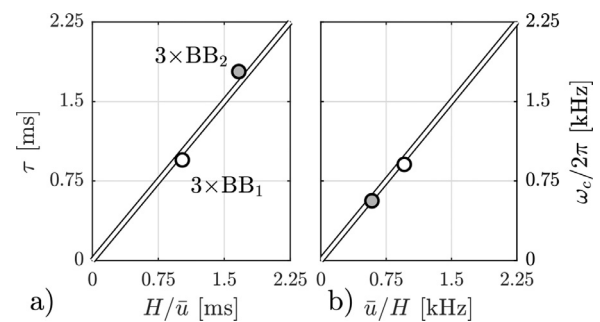


Fig. 12. Time delay and cut-off frequency extracted from the DTL model plotted against H/\bar{u} for the two symmetric cases with $3 \times BB_1$ and $3 \times BB_2$ bluff-body stabilised flames.

where DTL_a is the reconstructed FTF, DTL_{BB_1} and DTL_{BB_2} are the flame responses extracted from the cases with $3 \times BB_1$ and $3 \times BB_2$ stabilised flames respectively, and n_{BB_1} and n_{BB_2} are the number of flames stabilised with BB_1 and BB_2 in the reconstructed case. This relation follows directly from the acoustic mass continuity [52].

Using this method provides a very good representation of the measurements, showing that the total response is well approximated as a linear combination of the two symmetric responses. The trough in the asymmetric response occur when the phase difference between the two symmetric FTFs are half a cycle out of phase and is dependent on the relative time delays between the adjacent FTFs: $\tau_{BB_2} - \tau_{BB_1}$. Maximum suppression of the gain occurs when $f = 0.5/(\tau_{BB_2} - \tau_{BB_1})$, which in this case occurs at $f \approx 650\text{Hz}$.

This feature could be used to modify the response of the FTF by generating targeted interference between adjacent flames which is similar to the methods proposed by Noiray et al. [26] and Aesøy et al. [46]. If the frequency of an unstable mode is known, the difference in the convection time between the adjacent burners can be tuned such that the gain or phase is changed at that particular frequency. This strategy is similar to fuel staging [45], however here an asymmetry in the convection speed is targeted.

4. The nonlinear response

In the previous sections we focused on the linear flame response, which is sufficient to predict the onset of thermoacoustic instabilities through a linear stability analysis. However, it is insufficient to provide information about the saturation mechanism into a finite amplitude limit cycle which is a non-linear process [53]. In the next sections we investigate the effect of hydrogen enrichment and flame-flame interaction on self-excited limit cycle oscillations and the non-linear saturation of the flame response. In the following we only consider variations of P_H and d^* , with flames stabilised on the BB_1 bluff-body.

4.1. Self excited instability

To provoke self excited instabilities, the length of the combustion chamber L_c was increased and time series of pressure and HRR were recorded. In Fig. 14 the rms fluctuations of pressure and HRR are shown for different lengths L_c , for the different mixtures P_H . Data is only shown for $d^* = 2$, but a similar trend was observed for $d^* = 1.5$ and $d^* = 1.15$, which are not shown for brevity. Operation with a single flame was stable for all conditions, showing that the total thermal power needed to drive an instability is also important.

For $L_c = 50\text{mm}$ the combustor remains stable for all hydrogen contents. This was the reason for using the length for the forced measurements reported in the previous sections. For

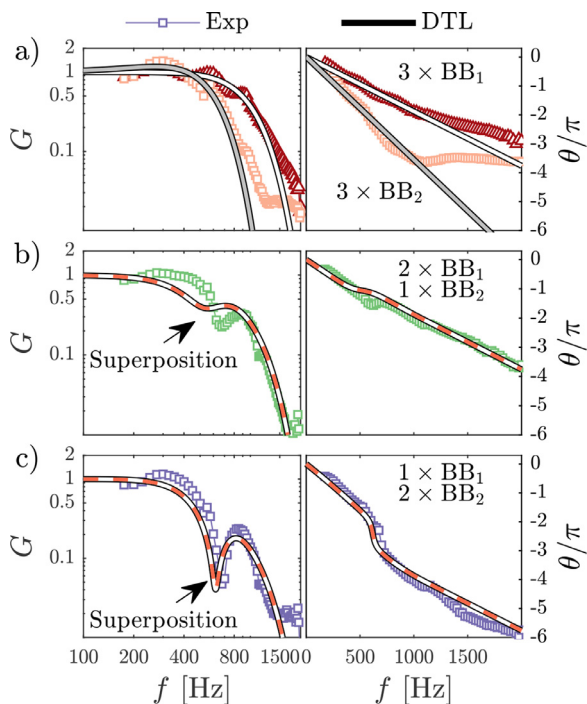


Fig. 13. FTFs for the different combinations of BB₁ and BB₂ stabilised flames shown in Fig. 5. a) shows the two symmetric cases and b) and c) show the two asymmetric cases. The DTL model is fitted to the symmetric cases (DTL_{BB₁} and DTL_{BB₂}) and in b) and c) the FTFs are reconstructed as a superposition of the two symmetric cases using Eq. (9).

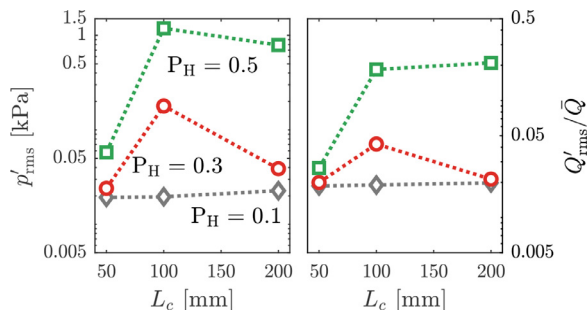


Fig. 14. Stability map showing rms fluctuations of pressure p_1 and HRR Q for $d^* = 2$ and different combustion chamber lengths L_c . The gray, red, and green colors indicate $P_H = 0.1, 0.3,$ and 0.5 respectively. (For interpretation of the references to color in this figure legend, the reader is referred to the web version of this article.)

$P_H = 0.1$, increasing L_c does not lead to a significant increase in the pressure and HRR amplitudes. For $P_H = 0.3$, the flame becomes marginally unstable for $L_c = 100\text{mm}$, and becomes stable again at $L_c = 200\text{mm}$. For $P_H = 0.5$, the flame becomes unstable at $L_c = 100\text{mm}$ and remains unstable as L_c is increased.

The appearance of a self-excited instability with increasing L_c is due to the increase of the cut-off frequency ω_c with increasing P_H . To show this, pressure spectra \hat{p} for different values of P_H and L_c are plotted in Fig. 15. The gray shaded regions correspond to the frequency range below the cut-off frequency ω_c which were obtained from the corresponding FTFs in Fig. 8. The figure shows that for all values of P_H , the peaks in the spectra for varying L_c only appear when they are close to or below $\omega_c/2\pi$. At $P_H = 0.1$, where $\omega_c/2\pi \approx 500\text{Hz}$, no unstable modes are observed and the spectra for all L_c overlap after the cut-off frequency. When P_H is increased to 0.3, the cut-off frequency $\omega_c/2\pi$ increases to around 1100Hz. As a result, a peak in the spectra appears near the cut-off frequency for $L_c = 100\text{mm}$, which corresponds to a self-excited instability at $f \approx 1200\text{Hz}$ for $L_c = 100\text{mm}$. Apart from the peak associated with

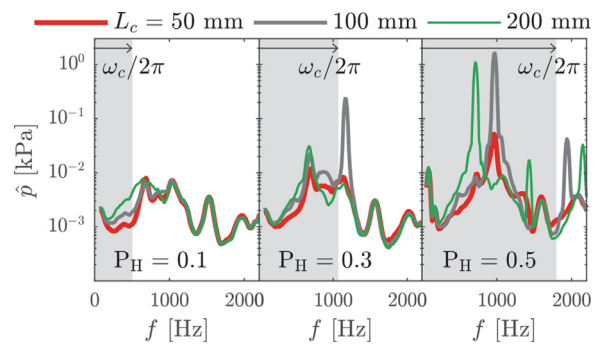


Fig. 15. Pressure spectra of p_1 for $d^* = 2$ with different combustion chamber lengths L_c and levels of hydrogen enrichment P_H . The gray regions indicate frequencies below the cut-off frequency $\omega_c/2\pi$ which were obtained from Fig. 8. P_H enrichment leads to an increase in the pressure fluctuations at higher frequencies due to an increase in $\omega_c/2\pi$.

the self-excited mode near the cut-off boundary, the spectra for all L_c collapse. When the level of hydrogen enrichment is increased further to $P_H = 0.5$, several unstable modes (and their harmonics) appear, at $f = 1000\text{Hz}$ for $L_c = 100\text{mm}$ and at $f = 740\text{Hz}$ at $L_c = 200\text{mm}$. These results indicate that premixed flames with increasing hydrogen enrichment can lead to more unstable modes at higher frequencies through an increase in the cut-off frequency.

This picture is consistent with the numerical study of the effect of hydrogen enrichment in laminar flames by Lim et al. [30]. They showed that as the level of hydrogen enrichment was increased, the fall off frequency of the gain was pushed to higher frequencies. The frequencies at which nonlinear effects became important were also increased. In the next section we show these latter effects are also observed but are slightly affected by flame-flame interactions.

To investigate how flame-flame interaction affects self-excited instabilities, we compare the time series taken for $d^* = 1.15$ and $d^* = 2$ at $L_c = 100\text{mm}$. In Fig. 16, we show phase portraits and the corresponding energy spectra of the pressure p_1 (a and b) and the global HRR (c and d). In a) and c) the phase portraits show the relationship between $p_1(t)$, $Q(t)$ and their time derivatives $\Delta p_1(t)/\Delta t$, $\Delta Q(t)/\Delta t$ which are obtained numerically. The scattered points show the instantaneous data for the full time series and the red and white lines show the phase averaged limit-cycle trajectories. The corresponding energy spectra are shown in Fig. 16 b) and d). The two limit-cycle trajectories and their energy spectra are very similar, showing that the effect of d^* on the amplitude and frequency is small. However, there is a slight tendency of lower saturation amplitude for smaller d^* , which is investigated through the Flame Describing Function (FDF) next.

4.2. The forced response

To investigate the effect of P_H and d^* on the non-linear response, a set of FDFs was measured at $f = 1000\text{Hz}$. This frequency was chosen for several reasons: 1) As shown in Fig. 15, the frequency was both beyond and below the cut-off frequency depending on P_H . 2) At $P_H = 0.5$, self-excited instability occurred close to this frequency when L_c was increased. 3) A strong response to forcing could be achieved at this frequency since it is close to a rig resonance, allowing for large velocity perturbations.

Fig. 17 shows the magnitude of $|\hat{Q}|/\hat{Q}$ as a function of the forcing level $|\hat{u}|/\bar{u}$. Different values of d^* are indicated by different markers, and the three mixtures are shown in green, red, and gray colors for $P_H = 0.5, 0.3,$ and 0.1 , respectively. The effect of P_H on the saturation amplitudes is significantly stronger than any differences due to a change in d^* although there is a trend towards saturation at lower amplitudes for increased flame-flame interaction,

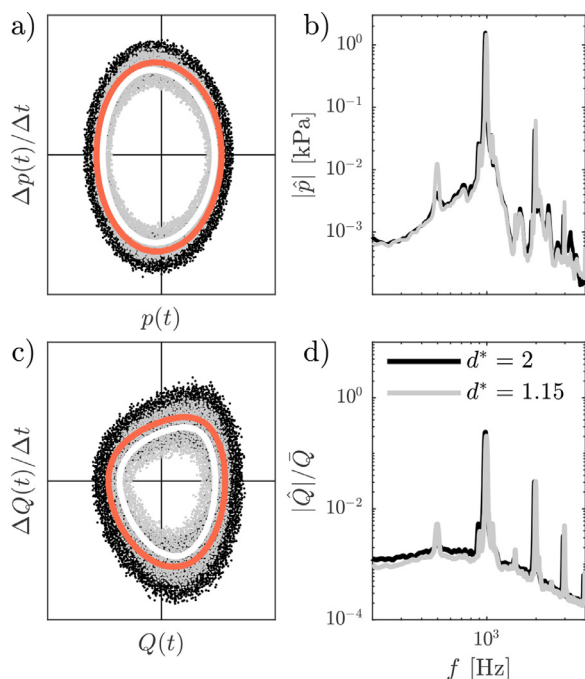


Fig. 16. Phase portraits and energy spectra of p_1 (a) and b)) and Q (c) and d)) for unstable limit-cycles observed at $P_H = 0.5$ for $d^* = 2$ and $d^* = 1.15$. a) and c) show phase portraits of the time series where the derivative is estimated numerically. The red and white lines indicate the phase averaged limit-cycle for $d^* = 2$ and 1.15 respectively. (For interpretation of the references to color in this figure legend, the reader is referred to the web version of this article.)

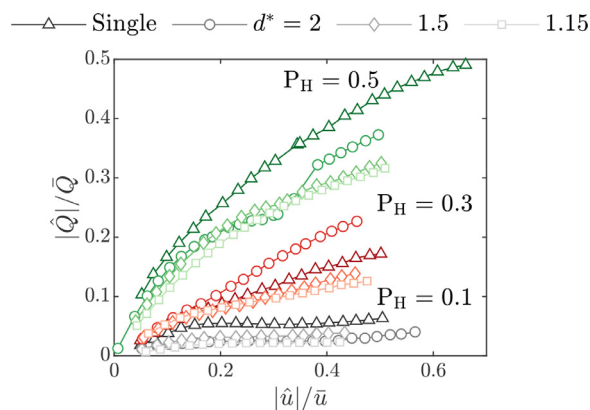


Fig. 17. FDFs measured at $f = 1000\text{Hz}$ for different values of P_H and d^* . Markers indicate different values of d^* and the gray, red, and green colors indicate $P_H = 0.1, 0.3,$ and 0.5 respectively. (For interpretation of the references to color in this figure legend, the reader is referred to the web version of this article.)

i.e. smaller values of d^* . This is consistent with the observation of the limit-cycle amplitudes in Fig. 16.

The large effect of P_H on the FDF is expected as the cut-off frequency increases with increasing P_H . At low values, as shown by the curves for $P_H = 0.1$, the forcing frequency is greater than the cut-off frequency, whereas at $P_H \geq 0.3$, the forcing frequency is at or below the cut-off frequency as previously shown in Fig. 15. Hence, when $P_H = 0.1$ the gain in the linear regime is already cut-off by the flame and thus the nonlinear response saturates at lower amplitudes. It is well known that the onset of a combustion instability is very sensitive to the time delay, i.e. the phase of the response quantified through the Rayleigh criterion [54]. Although the phase is a necessary condition, the nonlinear saturation of the response limits the amplitude of the HRR oscillations. As such, these results show that an increase of the hydrogen content leads to the potential of larger amplitude limit-cycles occurring at higher fre-

quencies compared to a methane flame at the same thermal power and equivalence ratio. This is consistent with what we observed in Figs. 14 and 15, where an increase in P_H lead to the onset of a self excited instability for both $L_c = 100\text{mm}$ and 200mm . It also explains the observations made in the literature where hydrogen enrichment has been shown to excite instabilities at higher frequencies compared to conventional fuels [5–12,14]. It should however be emphasised that an increase in P_H does not necessarily lead to an instability, but it increases the frequency range in which the flame response is large and thus, the possibility for one of the higher frequency modes to be excited.

5. Conclusions

In this paper we present a parametric study where the effect of hydrogen enrichment on the linear (FTF) and nonlinear (FDF) response of interacting flames in a simple model can combustor is studied. For the FTF, the effects of hydrogen enrichment, flame-flame interaction, wall confinement, and symmetry is investigated for both swirled and non-swirled flames. The cut-off frequency and time delay of the linear response is shown to shift linearly with the ratio between the flame length H and the bulk velocity \bar{u} for all cases. As was shown in a previous study by Æsøy et al. [19], hydrogen enrichment leads to more compact flames and a corresponding increase and decrease of the cut-off frequency and the time delay respectively. An increase of flame-flame interaction and confinement enhances the flame stability on the outer rim of the pipe, enforcing a 'M' shaped flame and thus a reduced flame length. The swirl stabilised flames had longer flame lengths, lower cut-off frequencies and shorter time delays compared to the corresponding non-swirled cases. The effects caused by wall confinement, flame-flame interaction, and swirl, change the FTF in a similar way as hydrogen enrichment by changing the distribution of HRR. However, the former effects are shown to be significantly weaker compared to a change in the hydrogen content. Furthermore, hydrogen enrichment leads to more compact flames where the effects of flame-flame interaction and wall confinement become less important.

The effect of having a collection of different flame holder geometries and hence, different convection velocities for adjacent flames are investigated. The FTFs of the asymmetric collections are shown to be well reproduced by a linear superposition of the measurements taken of the symmetric cases. By varying the time delay of adjacent flames, we produce interference which can potentially be used to tailor the flame response at selected frequencies providing a method to control instabilities. The effect shown here is similar to generating an asymmetry through fuel staging [45] or by generating targeted acoustic-convective interference [29,46]

Finally, the effects of hydrogen enrichment and flame-flame interaction on the non-linear flame saturation are investigated through measurements of self-excited instabilities and FDFs. When the length of the combustion chamber is increased, P_H enrichment leads to self-excited instabilities for a larger variety of frequencies and combustor lengths occurring with larger amplitudes. This occurs due to an increase in the cut-off frequency due to shorter flames which raises the potential of exciting modes at higher frequencies. The effect of flame-flame interaction is shown to have a small but significant effect on the saturation amplitude where more interaction tends to reduce the amplitude of the limit-cycle. These observations are consistent with the FDF measurements taken at a fixed forcing frequency where P_H enrichment leads to larger saturation amplitudes. Hence, hydrogen flames can potentially be more prone to generate large amplitude limit-cycle oscillations compared to methane flames. Furthermore, P_H enrichment leads to a reduced level of flame-flame interaction which is

expected to play a reduced role in the development of high hydrogen combustion systems such as those reported in [6–9,11].

Supplementary data set

Supplementary data sets for this article can be found online at <https://www.doi.org/10.5281/zenodo.6487687>

Declaration of Competing Interest

The authors declare that they have no known competing financial interests or personal relationships that could have appeared to influence the work reported in this paper.

Acknowledgments

The authors acknowledge support from the NCCS Centre, funded under the Norwegian research program, Centres for Environment-friendly Energy Research (FME) (Grant 257579/E20) and the European Union's Horizon 2020 research and innovation program ANNULIGHT (Grant 765998).

Appendix A. Estimate of flow rates with different bluff-bodies

Given the different blockage areas of the BB₁ and BB₂ bluff bodies and that each injector is fed from a common plenum, there is a difference in the pressure drop across each injector which will influence the thermal power of each flame. To investigate how the thermal power is distributed, we estimate the distribution of the HRR on each of the three flames by dividing the overhead image into three sectors as shown in Fig. A.18.

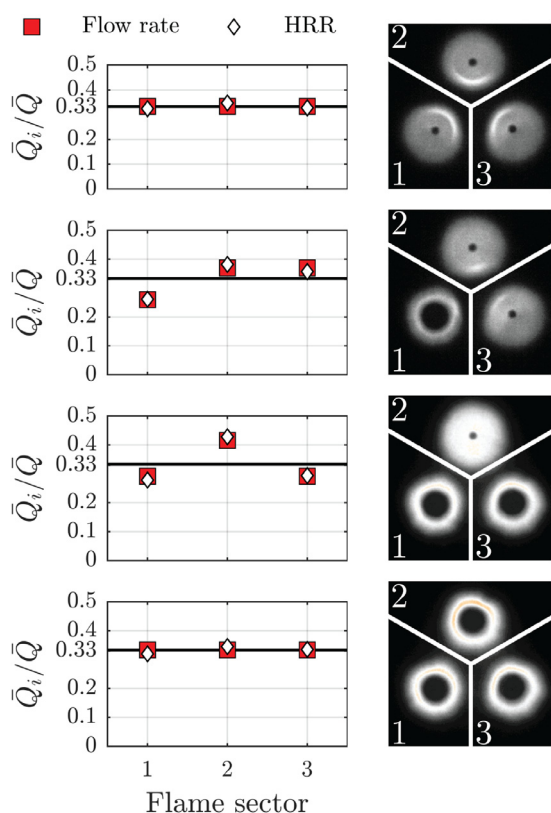


Fig. A.18. The overhead flame images shown in Fig. 11, divided into sectors covering each injector pipes. The plots on the left side show how much of the total HRR is distributed in each sector which are compared against the fraction of the total flow rate, estimated from a pipe network analysis.

The power distribution is estimated by integrating each sector \bar{Q}_i and dividing by the global HRR \bar{Q} , which is shown for each injector in the left part of the figure. These distributions were compared against the variation in the flow rate obtained using a simple pipe network analysis. The network consists of three pipes where a nozzle with a discharge coefficient $C_d = 0.98$ is added to one or two of the pipes. Solving for the flow rates and dividing by the total flow rate provides volume fractions which are shown by the red squares. These are in good agreement with the power fractions obtained from the images.

As expected, with three identical injectors, the flow rate and hence also the HRR are distributed equally between each injector. When the additional blockage of the BB₁ bluff-body is added, the flow rate through this injector is reduced slightly due to an increase in the pressure loss.

References

- [1] M.R. Bothien, A. Ciani, J.P. Wood, G. Fruechtel, Toward decarbonized power generation with gas turbines by using sequential combustion for burning hydrogen, *J. Eng. Gas Turb. Power* 141 (12) (2019).
- [2] T. Schuller, S. Marragou, G. Oztarliik, T. Poinso, L. Selle, Influence of hydrogen content and injection scheme on the describing function of swirled flames, *Combust. Flame* 240 (2022) 111974, doi:10.1016/j.combustflame.2021.111974.
- [3] G. Oztarliik, L. Selle, T. Poinso, T. Schuller, Suppression of instabilities of swirled premixed flames with minimal secondary hydrogen injection, *Combust. Flame* 214 (2020) 266–276.
- [4] T. Indlekofer, B. Ahn, Y.H. Kwah, S. Wiseman, M. Mazur, J.R. Dawson, N.A. Worth, The effect of hydrogen addition on the amplitude and harmonic response of azimuthal instabilities in a pressurized annular combustor, *Combust. Flame* 228 (2021) 375–387.
- [5] J.G. Aguilar, E. Æsøy, D.J. R. Predicting the influence of hydrogen in combustion instabilities, Symposium on Thermoacoustics in Combustion: Industry Meets Academia (SoTiC), Munich, Germany (2021), p. 9.
- [6] U. Jin, K.T. Kim, Experimental investigation of combustion dynamics and nox/co emissions from densely distributed lean-premixed multinozzle ch₄/c₃h₈/h₂/air flames, *Combust. Flame* 229 (2021) 111410.
- [7] T. Lee, K.T. Kim, High-frequency transverse combustion instabilities of lean-premixed multislit hydrogen-air flames, *Combust. Flame* 238 (2022) 111899.
- [8] J. Strollo, S. Peluso, J. O'Connor, Effect of hydrogen on steady-state and transient combustion instability characteristics, *J. Eng. Gas Turb. Power* 143 (7) (2021), doi:10.1115/1.4049481.
- [9] T. Lee, K.T. Kim, Combustion dynamics of lean fully-premixed hydrogen-air flames in a mesoscale multinozzle array, *Combust. Flame* 218 (2020) 234–246.
- [10] T. Indlekofer, A. Faure-Beaulieu, N. Noiray, J.R. Dawson, The effect of dynamic operating conditions on the thermoacoustic response of hydrogen rich flames in an annular combustor, *Combust. Flame* 223 (2021) 284–294, doi:10.1016/j.combustflame.2020.10.013.
- [11] H. Kang, K.T. Kim, Combustion dynamics of multi-element lean-premixed hydrogen-air flame ensemble, *Combust. Flame* 233 (2021) 111585.
- [12] J. Beita, M. Talibi, S. Sadasivuni, R. Balachandran, Thermoacoustic instability considerations for high hydrogen combustion in lean premixed gas turbine combustors: a review, *Hydrogen* 2 (1) (2021) 33–57.
- [13] E. Æsøy, The Effect of Hydrogen Enrichment on the Thermoacoustic Behaviour of Lean Premixed Flames, NTNU, 2022 Ph.D. thesis.
- [14] T. Indlekofer, The Dynamic Nature of Self-Excited Azimuthal Modes in Annular Combustors, NTNU, 2021 Ph.D. thesis.
- [15] T.C. Lieuwen, V. Yang, Combustion instabilities in gas turbine engines: operational experience, fundamental mechanisms, and modeling, *Amer. Inst. Aeronautics and Astronaut.*, 2005.
- [16] S. Ducruix, D. Durox, S. Candel, Theoretical and experimental determinations of the transfer function of a laminar premixed flame, *Proc. Combust. Inst.* 28 (1) (2000) 765–773.
- [17] C. Kulsheimer, H. Büchner, Combustion dynamics of turbulent swirling flames, *Combust. Flame* 131 (1–2) (2002) 70–84.
- [18] D. Durox, T. Schuller, N. Noiray, S. Candel, Experimental analysis of nonlinear flame transfer functions for different flame geometries, *Proc. Combust. Inst.* 32 (1) (2009) 1391–1398.
- [19] E. Æsøy, J.G. Aguilar, S. Wiseman, M.R. Bothien, N.A. Worth, J.R. Dawson, Scaling and prediction of transfer functions in lean premixed H₂/CH₄-flames, *Combust. Flame* 215 (2020) 269–282.
- [20] A. Kaufmann, F. Nicoud, T. Poinso, Flow forcing techniques for numerical simulation of combustion instabilities, *Combust. Flame* 131 (4) (2002) 371–385.
- [21] T. Schuller, D. Durox, S. Candel, A unified model for the prediction of laminar flame transfer functions: comparisons between conical and v-flame dynamics, *Combust. Flame* 134 (1–2) (2003) 21–34.
- [22] W. Polifke, C. Lawn, On the low-frequency limit of flame transfer functions, *Combust. Flame* 151 (3) (2007) 437–451.
- [23] A.P. Dowling, A kinematic model of a ducted flame, *J. Fluid Mech.* 394 (1999) 51–72.

- [24] T. Lieuwen, Modeling premixed combustion-acoustic wave interactions: a review, *J. Propuls. Power* 19 (5) (2003) 765–781.
- [25] Preetham, H. Santosh, T. Lieuwen, Dynamics of laminar premixed flames forced by harmonic velocity disturbances, *J. Propuls. Power* 24 (6) (2008) 1390–1402.
- [26] N. Noiray, D. Durox, T. Schuller, S.b. Candel, A novel strategy for passive control of combustion instabilities through modification of flame dynamics, *Turbo Expo: Power for Land, Sea, and Air*, volume 43130 (2008), pp. 1133–1144.
- [27] R. Balachandran, B.O. Ayoola, C.F. Kaminski, A.P. Dowling, E. Mastorakos, Experimental investigation of the nonlinear response of turbulent premixed flames to imposed inlet velocity oscillations, *Combust. Flame* 143 (1) (2005) 37–55, doi:10.1016/j.combustflame.2005.04.009.
- [28] B.D. Bellows, M.K. Bobba, J.M. Seitzman, T. Lieuwen, Nonlinear flame transfer function characteristics in a swirl-stabilized combustor, *J. Eng. Gas Turb. Power* 129 (4) (2007) 954–961, doi:10.1115/1.2720545.
- [29] E. Æsøy, J.G. Aguilar, M.R. Bothien, N. Worth, J. Dawson, Acoustic-convective interference in transfer functions of methane/hydrogen and pure hydrogen flames, *J. Eng. Gas Turb. Power* (2021), doi:10.1115/1.4051960.
- [30] Z. Lim, J. Li, A.S. Morgans, The effect of hydrogen enrichment on the forced response of $\text{CH}_4/\text{H}_2/\text{air}$ laminar flames, *Int. J. Hydrog.* (2021).
- [31] R. Tacina, C. Wey, P. Laing, A. Mansour, Sector tests of a low nox, lean-direct-injection, multipoint integrated module combustor concept, *Turbo Expo: Power for Land, Sea, and Air* volume 36061 (2002), pp. 533–544.
- [32] J. Cai, Aerodynamics of Lean Direct Injection Combustor with Multi-Swirl Arays, University of Cincinnati, 2006.
- [33] A.J. De Rosa, S.J. P. B.D. Quay, D.A. Santavicca, The effect of confinement on the structure and dynamic response of lean-premixed, swirl-stabilized flames, *J. Eng. Gas Turb. Power* 138 (6) (2016).
- [34] H.T. Nygård, N.A. Worth, Flame transfer functions and dynamics of a closely confined premixed body stabilised flame with swirl, *J. Eng. Gas Turb. Power* (2021), doi:10.1115/1.4049513.
- [35] N.A. Worth, J.R. Dawson, Cinematographic OH-PLIF measurements of two interacting turbulent premixed flames with and without acoustic forcing, *Combust. Flame* 159 (3) (2012) 1109–1126.
- [36] N.A. Worth, J.R. Dawson, Characterisation of flame surface annihilation events in self excited interacting flames, *Combust. Flame* 199 (2019) 338–351.
- [37] A. Tyagi, I. Boxx, S. Peluso, J. O'Connor, The role of flow interaction in flame-flame interaction events in a dual burner experiment, *Proc. Combust. Inst.* 37 (2) (2019) 2485–2491.
- [38] A. Tyagi, I. Boxx, S. Peluso, J. O'Connor, Statistics and topology of local flame-flame interactions in turbulent flames, *Combust. Flame* 203 (2019) 92–104.
- [39] A. Tyagi, I. Boxx, S. Peluso, J. O'Connor, Pocket formation and behavior in turbulent premixed flames, *Combust. Flame* 211 (2020) 312–324.
- [40] T. Lee, J. Park, D. Han, K.T. Kim, The dynamics of multiple interacting swirl-stabilized flames in a lean-premixed gas turbine combustor, *Proc. Combust. Inst.* 37 (4) (2019) 5137–5145.
- [41] T. Lee, J. Lee, J. Park, D. Han, K.T. Kim, Staggered swirler arrangement in two self-excited interacting swirl flames, *Combust. Flame* 198 (2018) 363–375.
- [42] D. Kim, J. Park, D. Han, K.T. Kim, Symmetry-breaking for the control of combustion instabilities of two interacting swirl-stabilized flames, *Combust. Flame* 194 (2018) 180–194.
- [43] M.T. Szedlmayer, B.D. Quay, J. Samarasinghe, A. De Rosa, J.G. Lee, D.A. Santavicca, Forced flame response of a lean premixed multi-nozzle can combustor, *Turbo Expo: Power for Land, Sea, and Air*, volume 54624 (2011), pp. 883–891.
- [44] J. Samarasinghe, S.J. Peluso, B.D. Quay, D.A. Santavicca, The three-dimensional structure of swirl-stabilized flames in a lean premixed multinozzle can combustor, *J. Eng. Gas Turb. Power* 138 (3) (2016).
- [45] J. Samarasinghe, W. Culler, B.D. Quay, D.A. Santavicca, J. O'Connor, The effect of fuel staging on the structure and instability characteristics of swirl-stabilized flames in a lean premixed multinozzle can combustor, *J. Eng. Gas Turb. Power* 139 (121504) (2017), doi:10.1115/1.4037461.
- [46] E. Æsøy, H.T. Nygård, N.A. Worth, J.R. Dawson, Tailoring the gain and phase of the flame transfer function through targeted convective-acoustic interference, *Combust. Flame* 236 (2022) 111813, doi:10.1016/j.combustflame.2021.111813.
- [47] B. Higgins, M. McQuay, F. Lacas, S. Candel, An experimental study on the effect of pressure and strain rate on CH chemiluminescence of premixed fuel-lean methane/air flames, *Fuel* 80 (11) (2001) 1583–1591.
- [48] A.F. Seybert, D.F. Ross, Experimental determination of acoustic properties using a two-microphone random-excitation technique, *J. Acoust* 61 (5) (1977) 1362–1370.
- [49] W. Polifke, C. Lawn, On the low-frequency limit of flame transfer functions, *Combust. Flame* 151 (3) (2007) 437–451.
- [50] T. Komarek, W. Polifke, Impact of swirl fluctuations on the flame response of a perfectly premixed swirl burner, *J. Eng. Gas Turb. Power* 132 (6) (2010), doi:10.1115/1.4000127.
- [51] P. Palies, D. Durox, T. Schuller, S. Candel, The combined dynamics of swirler and turbulent premixed swirling flames, *Combust. Flame* 157 (2010) 1698–1717, doi:10.1016/j.combustflame.2010.02.011.
- [52] M.R. Bothien, D. Wassmer, Impact of density discontinuities on the resonance frequency of Helmholtz resonators, *AIAA J.* 53 (4) (2015) 877–887, doi:10.2514/1.j053227.
- [53] N. Noiray, D. Durox, T. Schuller, S. Candel, A unified framework for nonlinear combustion instability analysis based on the flame describing function, *J. Fluid Mech.* 615 (2008) 139–167, doi:10.1017/S0022112008003613.
- [54] J.W. Strutt, *The Theory of Sound* volume 1, 1877.